RESEARCH ARTICLE

ADVANCED OPTICAL MATERIALS
www.advopticalmat.de

Light Intensity-Controlled Photoconductance Polarity Switching for Neuromorphic and Logic Applications

Amin Abnavi, Hamidreza Ghanbari, Mohammad Reza Mohammadzadeh, Ribwar Ahmadi, and Michael M. Adachi**

2D transition metal dichalcogenide (TMD) semiconductors and their heterostructures are widely studied for their positive photoconductance properties. Recent studies further explore the reversible modulation between positive photoconductance (PPC) and negative photoconductance (NPC), enabling applications in high-precision image recognition and bidirectional reconfigurable logic gates. However, the reversible photoconductance switching effect is commonly induced by different light wavelengths or gate voltages, which require multiple light sources or additional electronic components. Here, a photoconductance polarity switching effect is reported, induced by light intensity and duration in geometrically asymmetric *p*-type $MoSe_2$ devices. This effect arises from the asymmetric modulation of Schottky barrier heights due to the accumulation of photogenerated electrons at the $MoSe_2$/Cr interfaces. Additionally, a photosynaptic effect is observed, likely caused by the trapping/de-trapping of photogenerated carriers within the $MoSe_2$ crystal. Finally, a new type of reconfigurable logic gate with "OR" and "AND" functions is demonstrated in a single $MoSe_2$ device in which the light intensity and light-on duration from a single light source are the logic gate inputs, and the polarity of the output current determines the logic gate output.

1. Introduction

2D transition metal dichalcogenides, such as $MoSe_2$, have a high visible light absorption coefficient,[1] low dark current,[2] and fast carrier dynamics,[3] making them suitable for high-performance optoelectronic applications such as photodetectors,[4] solar cells,[3] and logic gates.[5] Conventional optoelectronic devices operate based on the positive photoconductance (PPC) effect,[6] in which light absorption enhances the electrical conductance of the material by generating additional charge carriers.[7] In contrast, the negative photoconductance (NPC) effect, which refers to the decrease in conductance when the material is exposed to light, has been reported in various inorganic (doped-Si, 2D materials), organic, and organic-inorganic hybrid semiconductor materials.[7,8]

Devices with tunable photoconductance polarity through external manipulation serve as new building blocks for next-generation optoelectronic systems.[9–12] The switchable photoconductance polarity is most commonly induced by different light wavelengths or gate voltages.[13–16] For example, Pi et al. have reported the gate-induced switchable photoconductivity in $PdSe_2/MoTe_2$ heterostructures for high-precision image recognition.[17] A gate-controlled polarity-reversible photodiode based on Top-In/WSe_2/Bottom-Au has also been reported for logic opto-electric switch application.[9] Kim et al. has also reported a multifunctional bidirectional logic gate based on back-to-back p^+-i-n-p-p^+ perovskite photodiodes with 100% accuracy in five logic operations.[18] The true and false states in the logic gates were distinguished by polarity rather than a threshold level, making the operations less susceptible to errors due to current fluctuations or electrical noise.[18]

Bipolar photoconductance controlled by light intensity offers a significant advantage over gate voltage or wavelength-controlled mechanisms by tuning the photoconductance polarity using a single wavelength and eliminating the need for additional electronic components.[19,20] Additionally, it enhances integration into all-optical systems and reduces operational complexity, paving the way for next-generation optoelectronic devices and artificial vision systems.[19,20] However, to the best of our knowledge, there are only three studies with light intensity-induced photoconductance polarity switching in the literature. Podborska et al reported photocurrent switching effect induced by light intensity in a photoelectrochemical system featuring a ternary hybrid material composed of ZnO, chloranilic acid, and fullerenols ($C_{60}(OH)_{30-36}$) within the electrolyte solution.[21] A field effect transistor (FET) based on graphene/InSe/h-BN heterojunction for image preprocessing also demonstrated the

A. Abnavi, H. Ghanbari, M. R. Mohammadzadeh, R. Ahmadi, M. M. Adachi
School of Engineering Science
Simon Fraser University
8888 University Drive
Burnaby, British Columbia V5A 1S6, Canada
E-mail: aabnavi@sfu.ca; mmadachi@sfu.ca

The ORCID identification number(s) for the author(s) of this article can be found under https://doi.org/10.1002/adom.202502227

DOI: 10.1002/adom.202502227

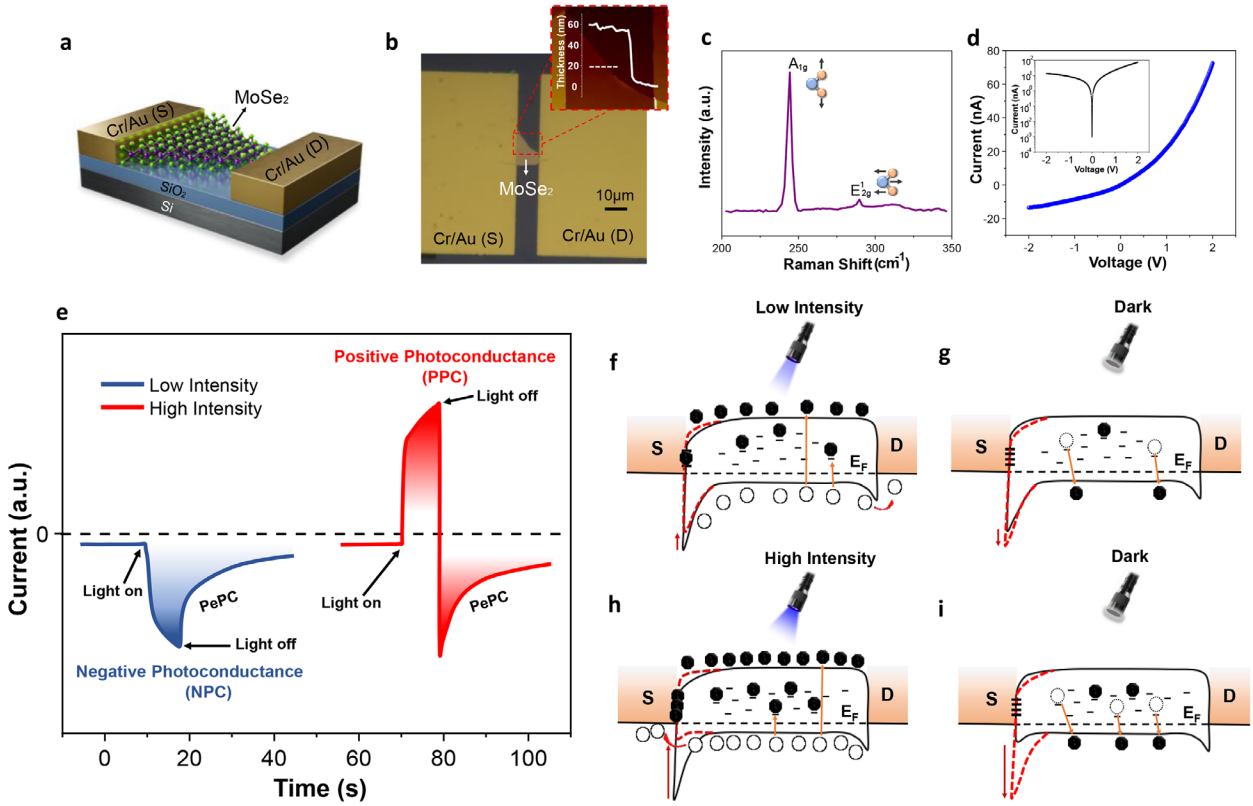

Figure 1. Light intensity-controlled photoconductance polarity switching in geometrically asymmetric $MoSe_2$ (GA-$MoSe_2$) Schottky photodiodes. a) The schematic illustration of the GA-$MoSe_2$ device with drain (labeled D) and source (labeled S) electrodes. b) The optical microscopy image of the GA-$MoSe_2$ device. Inset of (b) shows the AFM image of the $MoSe_2$ device (≈58 nm). c) Raman spectra of the $MoSe_2$ crystal, showing that it has semiconducting 2H-phase. d) The linear *I*–*V* characteristics of the GA-$MoSe_2$ device. Inset of (d) shows the corresponding logarithmic scale *I*–*V* characteristics, illustrating a current rectification of ≈6. e) Photoconductance polarity switching induced by light intensity. The low light intensity induces a negative photoconductance (NPC) effect, while the high-intensity illumination induces a positive photoconductance (PPC) effect in the GA-$MoSe_2$ device. The device shows a persistent photoconductivity (PePC) effect for both intensities. The energy band diagram of the Cr–$MoSe_2$–Cr structure under f) low light intensity, followed by g) dark conditions, and h) high light intensity, followed by i) dark conditions. The dashed red line indicates the modified Schottky barrier, while the red arrow illustrates the direction of its change.

light intensity-controlled photocurrent switching.[19] We also previously reported a photovoltaic switching effect induced by light intensity in geometrically asymmetric *n*-type MoS_2 Schottky devices. Bidirectional optoelectronic logic gates were demonstrated based on light intensity and gate bias as the logic gate inputs, and polarity of the output current polarity as the logic gate output.[20]

Here, we demonstrate a light intensity-controlled photoconductance polarity switching in geometrically asymmetric *p*-type $MoSe_2$ devices (GA-$MoSe_2$). This effect can be attributed to the accumulation/trapping of photogenerated electrons at the $MoSe_2$/Cr interfaces, which results in the asymmetric lowering of the Schottky barrier heights and a change in the direction of carrier collection. A persistent photoconductivity effect is also observed in these devices, which could be due to the trapping/de-trapping of photogenerated carriers within the $MoSe_2$ crystal. The paired-pulse facilitation (PPF) of ≈150% is achieved for the high-intensity light (PPC mode), which is much higher than that of the low-intensity light (NPC mode, ≈109%). We finally demonstrate a new type of reconfigurable optical logic gate capable of performing "OR" and "AND" operations using a single light source with tunable intensity and duration.

2. Results And Discussion

GA-$MoSe_2$ devices were fabricated using mechanically exfoliated crystals. Figure S1 (Supporting Information) illustrates the fabrication process of the GA-$MoSe_2$ devices. The schematic illustration and optical image of the GA-$MoSe_2$ device are shown in **Figure** 1a,b, respectively. The device consists of a $MoSe_2$ flake with two asymmetric $MoSe_2$/Cr contact areas at drain and source electrodes. The $MoSe_2$ crystal has a thickness of ≈58 nm, determined by atomic force microscopy (AFM, inset of Figure 1b). Raman spectroscopy of the $MoSe_2$ flake exhibits two distinct peaks: a prominent peak at 244 cm^{-1} corresponding to the out-of-plane vibration mode (A_{1g}) and a weaker peak at 285 cm^{-1} associated with the in-plane vibration mode (E^1_{2g}), verifying the 2H semiconducting phase of $MoSe_2$.[22] (Figure 1c).

The linear current–voltage (*I*–*V*) curve of the GA-$MoSe_2$ device is illustrated in Figure 1d, showing a current rectification ratio of ≈6, measured at bias voltages of ±1 V without gate bias. Inset

of Figure 1d shows the corresponding logarithmic *I*–*V* curve. In our previous studies, we demonstrated that the current rectification ratio can be controlled by the degree of asymmetry and thickness of 2D flakes.[23,24] The rectifying behavior observed in devices with asymmetric architectures is attributed to the asymmetric Schottky barriers formed at the $MoSe_2$/Cr interfaces due to the interface states.[23]

Figure 1e shows the current–time (*I*–*t*) characteristics of the GA-$MoSe_2$ device under low and high light intensities. At low and high light intensities, the device shows the NPC and PPC behaviors, respectively, exhibiting a photoconductance polarity switching effect (Figure 1e). We propose that this switching behavior is attributed to the Schottky barriers modulation due to the electron trapping/accumulation at the $MoSe_2$/Cr interfaces. A persistent photoconductivity effect (PePC), also known as photosynaptic effect, where the photo-enhanced conductivity remains after removing the light,[25,26] is also observed for both low and high light intensities, which is likely due to the trapping/de-trapping of photogenerated electrons in the $MoSe_2$ defect states.[27]

To explain the physical mechanism behind the NPC to PPC switching and PePC effects, we use the energy band diagram of Cr-$MoSe_2$-Cr structure. The transfer curve of the symmetric $MoSe_2$ device indicates its *p*-type behavior (Figure S2, Supporting Information). The GA-$MoSe_2$ is proposed to form two asymmetric Schottky barriers at the interfaces with a larger Schottky barrier at the larger $MoSe_2$/Cr interface[23] (Figure 1f–i). At low light intensity, the generation of electrons is insufficient to saturate the available surface states and can not significantly reduce the Schottky barriers at the drain interface. Therefore, the generated holes flow to the smaller interface (Figure 1f), producing a sharp negative photocurrent (Figure 1e). Meanwhile, some of the generated electrons become trapped in the deep defect states within the $MoSe_2$ flake, resulting in a gradual increase in the conductivity of the device under light exposure.[28] When the light is off, the trapped electrons are slowly recombined (Figure 1g) and result in a PePC effect[29] (Figure 1e).

At high light intensity, a significant number of generated electrons are trapped at the $MoSe_2$/Cr interfaces, leading to an uneven reduction of the Schottky barriers,[30,31] with the larger $MoSe_2$/Cr interface being more affected due to the larger contact area and higher concentration of interface states[20,32] (Figure 1h). This modulation in the energy band alignment of the Cr–$MoSe_2$–Cr structure results in a photocurrent with reversed polarity (Figure 1e). When the light is turned off, the Schottky barrier at the larger interface instantly returns to its initial level as trapped electrons are released from the interface (Figure 1i). Simultaneously, electrons trapped in deep states within the $MoSe_2$ channel are slowly released (Figure 1i), altering the conductivity of the $MoSe_2$ channel and resulting in a long PePC effect[28] (Figure 1e). Since higher light intensity leads to the generation and trapping of more electrons, the decay of the PePC effect is longer than that of low light intensity.[27] Other factors, such as the distribution and density of defect states in $MoSe_2$ and differences in carrier recombination dynamics under excitation, can also affect electron trapping and the photocurrent switching effect. Figure S3 (Supporting Information) shows the cycling measurements between low and high light intensities, indicating that the modulation of Schottky barriers at the interfaces by electron trapping is reversible.

To further investigate this switching phenomenon, the *I*–*t* characteristics of the GA-$MoSe_2$ device were measured at varying light intensities, ranging from 88 μW cm^{-2} to 3.7 mW cm^{-2}, with a constant illumination duration of 5 s. The results reveal a transition from NPC to PPC effect as the light intensity increases (**Figure 2a**). At high light intensity (3.7 mW cm^{-2}), a significant number of photogenerated electrons are rapidly trapped at the larger interface, leading to the Schottky barrier lowering and a strong positive photocurrent (Figure 2a). The detailed transition from NPC to PPC as a function of light intensity is shown in Figure S4 (Supporting Information). The photoconductance switching effect is not observed, even under a high light intensity of up to 16 mW cm^{-2}, when the device exhibits a high current rectification ratio (e.g., 10^4),[23] which could be due to the dominant influence of the strong built-in potential.[20]

The duration of the light pulse is another important factor that can affect the photoconductance switching behavior. With low intensity (88 μW cm^{-2}), the photocurrent polarity remains unchanged across different light durations from 50 ms to 5 s (Figure S5, Supporting Information). In this case, even with the longest light duration, the number of generated electrons is insufficient to lower the Schottky barrier and reverse the photocurrent. Conversely, at high light intensity, the duration of light can alter the photoconductance polarity of the device (Figure 2b). At shorter durations, the number of photogenerated electrons is insufficient to occupy the surface states at the larger $MoSe_2$/Cr interface and lower the Schottky barrier, resulting in an NPC effect. Thus, both light intensity and light-on duration can modulate and switch the photoconductance polarity.

As shown in Figure 2, when the light is turned off, the current gradually returns to its initial level. This recovery process can be modulated by adjusting the light intensity and duration, making the device suitable for artificial synapse applications.[33] In biological neural systems, a synapse is a narrow junction through which electrical or chemical signals are transmitted from a pre-synaptic neuron to a post-synaptic neuron. Similarly, in our optoelectronic GA-$MoSe_2$ device, light pulses act as pre-synaptic stimuli, while the output current (I_{out}) is regarded as the post-synaptic response. A schematic representation of a biological synapse alongside our GA-$MoSe_2$ synaptic device is presented in **Figure 3a**. Key synaptic functions such as excitatory post-synaptic current (EPSC), PPF, and the transition from short-term memory (STM) to long-term memory (LTM),[34] have been successfully demonstrated through light pulse stimulation. EPSC refers to the change in current (I_{out}), which is influenced by the duration, intensity, and number of the input light pulses. The modulation in light intensity and duration can be used to transition the device from STM to LTM characteristics at zero bias (Figure S6, Supporting Information). If the applied bias voltage is sufficiently large, it can transform the device into a unidirectional synaptic device, eliminating the transition from NPC to PPC (Figure S7, Supporting Information). The synaptic response of the GA-$MoSe_2$ device is primarily attributed to the trapping and de-trapping of photogenerated carriers, either in the $MoSe_2$ crystal or at the SiO_2/$MoSe_2$ interface.[35] However, the photosynaptic behavior was also observed in the devices fabricated on PET and Al_2O_3 substrates (Figure S8, Supporting Information), which indicates the dominant mechanism is likely the trapping and de-trapping of photogenerated carriers within the $MoSe_2$ crystal rather than substrate-related effects. The

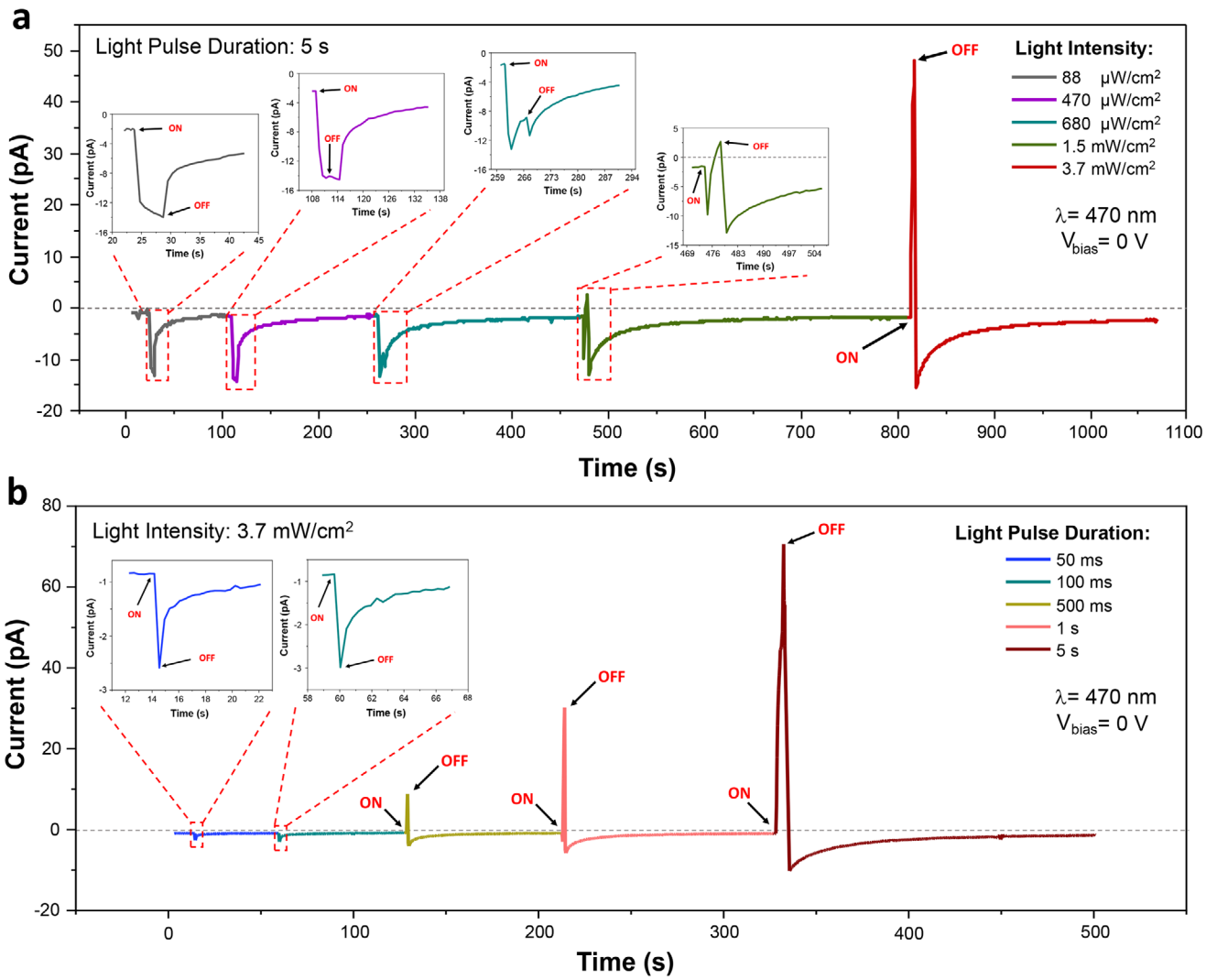

Figure 2. Tunability of the photoconductance polarity switching via light intensity and light-on duration. a) The photoresponse of the GA-$MoSe_2$ device as a function of light intensity. b) The photoresponse of the GA-$MoSe_2$ device as a function of light pulse duration under high light intensity of 3.7 mW cm^{-2}.

photocurrent switching effect is further demonstrated in additional GA-$MoSe_2$ devices (Figure S9, Supporting Information). The photosynaptic behavior remains device-dependent, which is attributed to variations in defect concentrations across different flakes. On the other hand, the symmetric $MoSe_2$ devices show negligible current rectification ratio with a net photocurrent of about zero under illumination (Figure S10, Supporting Information).

To further explore the plasticity behavior, the photocurrent for 1, 2, 5, 10, and 50 sequential light pulses with a 2.5 s duration, and intensities of 88 μW cm^{-2} and 3.7 mW cm^{-2} are shown in Figure 3b,c. For a single pulse, the current returns to its initial state in a short time of less than 100 s, which shows STM characteristics. The current decays more slowly with an increasing number of sequential light pulses, with the slowest decay observed when 50 pulses are applied (Figure 3b,c). This behavior demonstrates the transition from STM to LTM as the number of light pulses increases (Figure S11, Supporting Information). The PPF index is defined as the ratio of A_2 to A_1, where A_2 and A_1 represent the current amplitudes generated by two consecutive light pulses separated by an interval duration Δt,[36] as shown in the inset of Figure 3d,e. A PPF index greater than 1 indicates that the current amplitude induced by the second pulse is larger than that of the first pulse. The PPFs are ≈109% and ≈150% for the low (NPC mode) and high (PPC mode) light intensities of 88 μW cm^{-2} and 3.7 mW cm^{-2}, respectively, at the shortest pulse interval of 500 ms (Figure 3d,e). The PPFs decrease gradually to ≈100% and ≈112% with the increase in the time interval to 4 s. The corresponding photoresponses for several Δt are shown in Figure S12 (Supporting Information). A higher PPF index at the PPC mode indicates better mimicry of biological synaptic behavior.[37] In biological synapses, the ability to recognize and interpret visual information in real time heavily depends on the PPF behavior of postsynaptic neurons.[38] Therefore, developing optoelectronic synaptic devices with an enhanced PPF index is vital for driving progress in artificial vision technologies.[37] Moreover, the devices with controllable *I–t* temporal dynamics, such as the GA-$MoSe_2$ device, can also be used

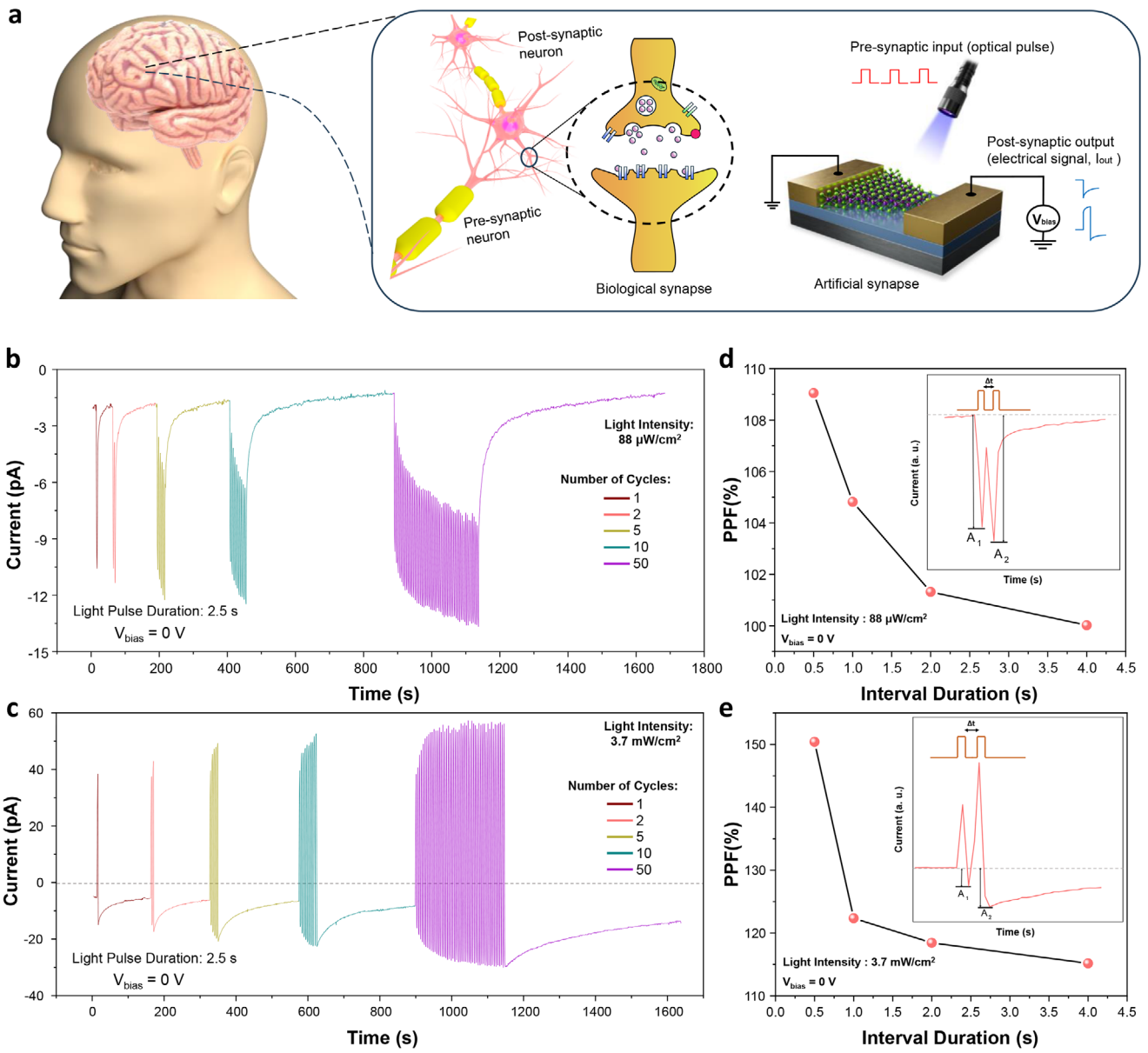

Figure 3. The photosynaptic characteristics of the GA-$MoSe_2$ device. a) Schematic of a biological synapse in the human brain and the GA-$MoSe_2$ device as an artificial bidirectional synapse. The photoresponse of the GA-$MoSe_2$ device as a function of the number of light pulses (1 to 50 pulses) with b) low light intensity (88 μW cm^{-2}) and c) high light intensity (3.7 mW cm^{-2}). The PPF of the GA-$MoSe_2$ device as a function of interval duration, Δt, between two consecutive light pulses with d) low light intensity (88 μW cm^{-2}) and e) high light intensity (3.7 mW cm^{-2}).

for multimode reservoir computing and hierarchical information processing.[39,40]

The light intensity-induced photoconductance polarity switching in this work is attributed to the Schottky barrier modulation due to the electron trapping effect. To further examine this mechanism in the GA-$MoSe_2$ device, photocurrent 2D profiling was performed under background illumination with both low and high light intensities (**Figure 4**). A laser beam (λ = 485 nm, d = 1 μm) was moved across the device from the larger $MoSe_2$/Cr interface to the smaller one with a step size of 1 μm. Under low background illumination (0.5 mW cm^{-2}), electron trapping and Schottky barrier lowering are minimal (Figure 4a), resulting in a larger photocurrent at the smaller interface and therefore a negative net photocurrent (Figure 4b). However, under high-intensity background illumination, the Schottky barrier lowering at the larger interface becomes significant (Figure 4c), leading to a larger photocurrent at the larger interface and a positive net photocurrent (Figure 4d). This behavior suggests that the light intensity-induced switching of photoconductance polarity is primarily driven by electron trapping and Schottky barrier lowering at the larger $MoSe_2$/Cr interface. Note that the peak photocurrents show that the laser is at the edge of the $MoSe_2$/Cr interface, and when the laser beam moves on the electrode, the photocurrent drops considerably. A symmetric $MoSe_2$ device shows a

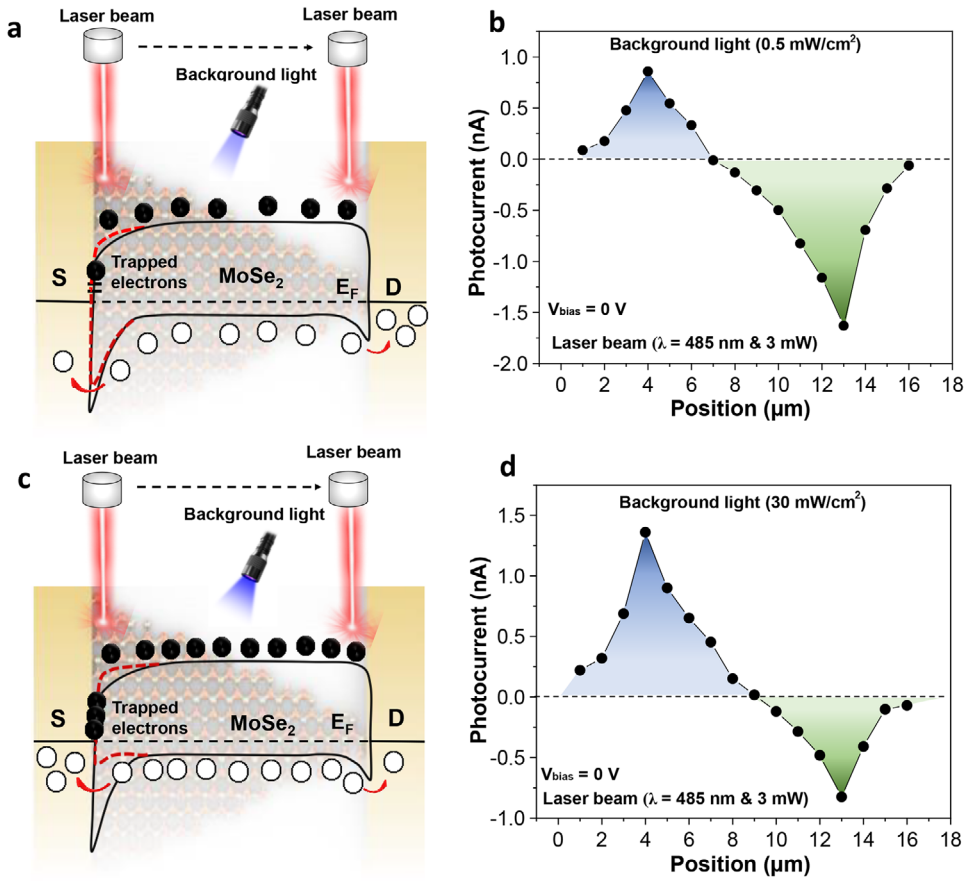

Figure 4. The working mechanism of the light intensity-controlled photoconductance switching effect. The energy band diagram of the GA-$MoSe_2$ device under background light with a) low and b) high intensities. A laser beam spot with a diameter of 1 μm is scanned across the device from the larger to the smaller Cr-$MoSe_2$ interface. The photocurrent of the device as a function of laser beam position with a background light with c) low and d) high light intensities. Note that the background light illuminates the entire device area.

bidirectional symmetric photocurrent across the device,[23] which results in a net photocurrent of about zero when the entire device is under illumination. The temperature-dependent *I–V* characteristics of a GA-$MoSe_2$ device show negligible V_{oc} and I_{sc} under high temperature and dark conditions (Figure S13, Supporting Information), ruling out the photothermoelectric effect as the main mechanism behind the photocurrent switching.[41]

The GA-$MoSe_2$ device, with its light intensity- and duration-induced switchable photocurrent polarity, has great potential for application in reconfigurable bidirectional optoelectronic logic gates (**Figure 5**). Optical modulation of logic gates presents several benefits over electrical modulation, such as its simplicity and easier integration with silicon photonic devices.[42] It also generates less heat and reduces electromagnetic interference,[43] which can result in optoelectronic devices with higher integration density and enhanced performance.

In this system, two logical inputs are encoded within a single optical signal, where intensity defines *Input A* and duration defines *Input B*. The output polarity of the device directly represents the binary state, enabling "OR" and "AND" logic operations with a single light source. We adjusted the light intensity by varying the distance between the light source and the GA-$MoSe_2$ device, while the duration of the light was controlled using a function generator. However, the light intensity and duration can also be tuned by a neutral density filter and an optical chopper, respectively, as illustrated in Figure 5a. The light intensity represents the input A, where a low light intensity (I_{in} = 4.1 mW cm^{-2}) corresponds to binary state "0" and a higher light intensity (I_{in} = 6.5 mW cm^{-2}) corresponds to the binary state "1". The light-on duration represents input B, where a short duration (D_{in} = 100 ms) corresponds to binary state "0," and a long duration (D_{in} = 500 ms) corresponds to binary state "1". The polarity of output current (I_{out}) can determine the true and false states, where negative photocurrent corresponds to state "0" and positive photocurrent to state "1". It has been demonstrated that multifunctional logic gate operations based on the photocurrent polarity rather than relative difference in unipolar photocurrent are insusceptible to electrical noise or current variation between pixels, demonstrating gate operations with 100% accuracy.[18] The applied bias voltage (V_{bias}) can be used as a programming input to switch the logic gate operations between "OR" and "AND" (Figure 5b). When V_{bias} = 0, the device performs an "OR" operation, and V_{bias} = −0.8 mV it performs an "AND" operation. The I_{out}-t characteristics of the device for different input binary states and V_{bias} = 0 V are shown in Figure 5c–f, illustrating the "OR" logic operation.

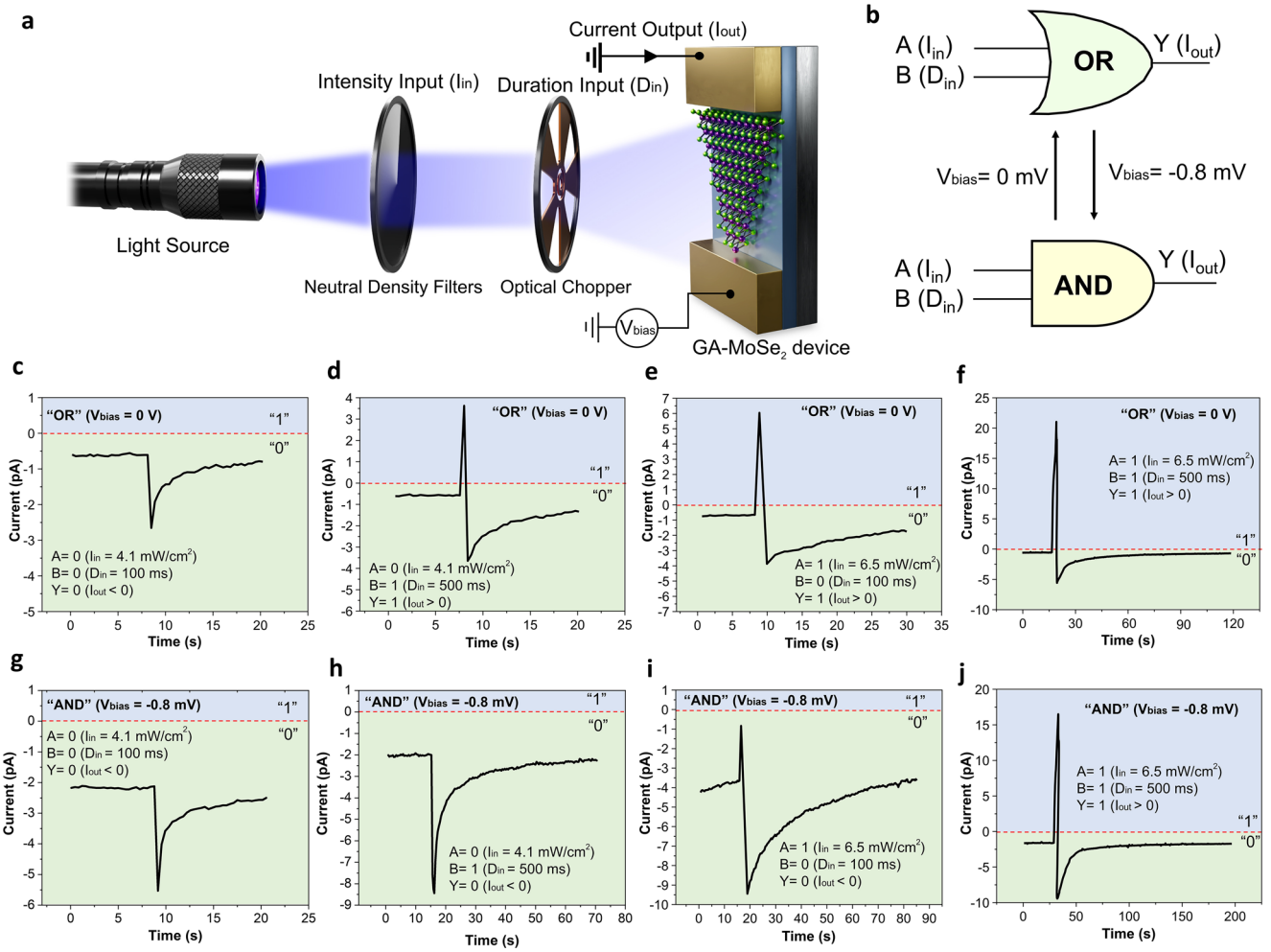

Figure 5. The optoelectronic bidirectional logic gate application of the GA-$MoSe_2$ device. a) The schematic illustration of the GA-$MoSe_2$ device and its optical input. The light intensity can be controlled with a neutral density filter, and the light duration can be controlled with a chopper. b) The diagram of the reconfigurable "OR" and "AND" logic gates. Two logic gate inputs are A, represented by the light intensity, I_{in}, (A = 0 if I_{in} = *4.1* mW cm^{-2} and A = 1 if I_{in} = *6.5* mW cm^{-2}) and B, represented by light-on duration, D_{in}, (B = 0 if D_{in} = *100* ms and B = 1 if D_{in} = 500 ms) of a single light source. The logic gate output, Y, is determined by the polarity of the output current I_{out} (Y = 0 if I_{out} < 0 and Y = 1 if I_{out} > 0). c–f) The I_{out}-t characteristics of the GA-$MoSe_2$ device showing an "OR" operation when V_{bias} = 0 V. g–j) The I_{out}-t characteristics of the GA-$MoSe_2$ device showing an "AND" operation when V_{bias} = −0.8 mV.

When V_{bias} = −0.8 mV, the device operation changes to "AND" (Figure 5g–j), demonstrating reconfigurable logic gates.

Conventional logic gates are purely electronic, relying on electrical signals for logic operations.[44] Optoelectronic logic gates, on the other hand, leverage light-matter interactions and process optical signals to perform logical operations such as AND, OR, and NOT, making them ideal for photonic circuits and applications requiring high-speed and parallel data processing.[45] However, traditional optoelectronic logic gates are mostly limited to performing a single logic function per device due to the unidirectional nature of photocurrent in conventional solid-state devices.[46] The ability to switch between functions such as "OR" and "AND" operations within a single device is a key feature of reconfigurable logic gates.[47,48] Photocurrent polarity-switchable or bidirectional logic devices can provide multifunctionality, enabling multiple operations within a single device.[49] Bidirectional logic gates can identify true or false states based on polarity rather than a threshold level, improving the accuracy of logic operations by reducing sensitivity to current fluctuations and electrical noise.[18] The geometrically asymmetric devices offer potential for scalable fabrication, utilizing top-down approaches such as wafer-scale growth of 2D materials,[50] followed by precise patterning, etching, lithography, and metal evaporation.[24]

3. Conclusion

We have demonstrated that the light intensity and duration can control the photoconductance polarity of the geometrically asymmetric $MoSe_2$ devices. This phenomenon could be explained by the Schottky barrier modulation at the $MoSe_2$/Cr interfaces under light illumination due to electron trapping/accumulation. A persistent photoconductivity effect, attributed to the trapping and de-trapping of photogenerated electrons within the $MoSe_2$ crystal, offers potential for artificial synaptic applications with

controllable temporal dynamics. Finally, a proof-of-concept bidirectional and reconfigurable optoelectronic logic gate capable of performing "OR" and "AND" operations was successfully demonstrated in a $MoSe_2$ device using a single light source with tunable intensity and duration.

4. Experimental Section

Preparation of Geometrically Asymmetric Multilayer $MoSe_2$ Devices: $MoSe_2$ flakes were obtained on a SiO_2/Si substrate via mechanical exfoliation from a bulk $MoSe_2$ crystal, grown by the chemical vapor transport (CVT) method (2D Semiconductors), using Nitto SPV224 tape. Triangular $MoSe_2$ crystals, chosen for their significant variation in contact area between the drain and source sides, were selected, and Cr/Au (10/60 nm) electrodes were then patterned onto the flakes using photolithography. This was followed by thermal evaporation and a lift-off process in an acetone bath. A schematic of this fabrication process is shown in Figure S1 (Supporting Information). The GA-$MoSe_2$ devices were similarly fabricated on the PET and Al_2O_3 substrates.

Material Characterization: The morphology and thickness of the $MoSe_2$ flakes were characterized using atomic force microscopy (AFM, Asylum MFP-3D). Raman spectroscopy of the GA-$MoSe_2$ sample was performed using a Renishaw inVia confocal Raman microscope, which was equipped with a 514 nm continuous-wave excitation laser.

Electrical/Optical Characterization: Electrical measurements were conducted using a Keithley 4200-SCS semiconductor characterization system connected to a chamber. An LED with a wavelength of 470 nm was used as the light source. A function generator (Tektronix AFG3151C) connected to the 470 nm LED was used to generate optical pulses with controllable durations. Photocurrent profiling was performed using a motorized X–Y stage with 1 µm resolution accuracy, scanning the devices under a pulsed 485 nm laser focused through a 50× objective lens. During testing, the device was positioned at the center of the illumination area to ensure consistency and maximize illumination uniformity. All measurements were conducted at room temperature and atmospheric pressure.

Supporting Information

Supporting Information is available from the Wiley Online Library or from the author.

Acknowledgements

This work was supported by the Natural Sciences and Engineering Research Council of Canada (NSERC), Canada Foundation for Innovation (CFI), British Columbia Knowledge Development Fund (BCKDF), Western Economic Diversification Canada (WD), and Simon Fraser University. The authors thank B. Kim for maintenance of the SFU Engineering Science cleanroom facility, Dr. D. Leznoff for access to Raman microscopy, Dr. Amirhossein Hasani and Mr. Ehsan Faridi for designing the figures' schematics. The authors would also like to thank Mirette Fawzy, Thushani De Silva, Fahmid Kabir, and Prof. Deji Akinwande for their helpful discussions. The authors acknowledge CMC Microsystems and 4D LABS shared facilities that facilitated this research.

Conflict of Interest

The authors declare no conflict of interest.

Author Contributions

A.A. and H.G. contributed equally to this work. A.A. and H.G. performed all experimental design, fabrication, and measurements under the supervision of M.M.A. M.R.M. conducted the AFM characterizations and designed the synapse schematics. M.R.M. and R.A. participated in data analysis and scientific discussions. A.A. and H.G. wrote the manuscript. All authors contributed to manuscript editing. M.M.A. edited the manuscript, supervised the project, and assisted with data analysis and manuscript preparation.

Data Availability Statement

The data that support the findings of this study are available from the corresponding author upon reasonable request.

Keywords

2D $MoSe_2$, bidirectional logic gate, bidirectional optical synapse, neuromorphic, photoconductance switching

Received: July 10, 2025
Revised: September 14, 2025
Published online:

[1] A. Asaithambi, N. Kazemi Tofighi, N. Curreli, M. De Franco, A. Patra, N. Petrini, D. Baranov, L. Manna, F. D. Stasio, I. Kriegel, *Adv. Opt. Mater.* **2022**, *10*, 2200638.
[2] X. Geng, Y. Yu, X. Zhou, C. Wang, K. Xu, Y. Zhang, C. Wu, L. Wang, Y. Jiang, Q. Yang, *Nano Res.* **2016**, *9*, 2641.
[3] G. Wang, Z. Guo, C. Chen, W. Yu, B. Xu, B. Lin, *Sol. Energy* **2022**, *236*, 576.
[4] H. Xue, Y. Wang, Y. Dai, W. Kim, H. Jussila, M. Qi, J. Susoma, Z. Ren, Q. Dai, J. Zhao, *Adv. Funct. Mater.* **2018**, *28*, 1804388.
[5] M. C. Sahu, S. Sahoo, S. K. Mallik, A. K. Jena, S. Sahoo, *Adv. Mater. Technol.* **2023**, *8*, 2201125.
[6] H. Zhang, H. Li, F. Wang, X. Song, Z. Xu, D. Wei, J. Zhang, Z. Dai, Y. Ren, Y. Ye, *ACS Appl. Electron. Mater.* **2022**, *4*, 5177.
[7] N. K. Tailor, C. A. Aranda, M. Saliba, S. Satapathi, *ACS Mater. Lett.* **2022**, *4*, 2298.
[8] M. A. Haque, J. L. Li, A. L. Abdelhady, M. I. Saidaminov, D. Baran, O. M. Bakr, S. H. Wei, T. Wu, *Adv. Opt. Mater.* **2019**, *7*, 1900865.
[9] J. Du, Q. Liao, B. Liu, X. Zhang, H. Yu, Y. Ou, J. Xiao, Z. Kang, H. Si, Z. Zhang, *Adv. Funct. Mater.* **2021**, *31*, 2007559.
[10] Y. Cheng, J. Ye, L. Lai, S. Fang, D. Guo, *Adv. Electron. Mater.* **2023**, *9*, 2201216.
[11] H. Xu, Y. Weng, K. Chen, C. Wu, H. Hu, D. Guo, *Adv. Opt. Mater.* **2025**, *13*, 2402238.
[12] J. Ye, S. Jin, Y. Cheng, H. Xu, C. Wu, F. Wu, D. Guo, *ACS Appl. Mater. Interfaces* **2024**, *16*, 26512.
[13] L. Mennel, J. Symonowicz, S. Wachter, D. K. Polyushkin, A. J. Molina-Mendoza, T. Mueller, *Nature* **2020**, *579*, 62.
[14] J. Han, J. Wang, M. Yang, X. Kong, X. Chen, Z. Huang, H. Guo, J. Gou, S. Tao, Z. Liu, *Adv. Mater.* **2018**, *30*, 1804020.
[15] D. Wang, X. Liu, Y. Kang, X. Wang, Y. Wu, S. Fang, H. Yu, M. H. Memon, H. Zhang, W. Hu, *Nat. Electron.* **2021**, *4*, 645.
[16] S. Fang, L. Li, W. Wang, W. Chen, D. Wang, Y. Kang, X. Liu, H. Jia, Y. Luo, H. Yu, *Adv. Mater.* **2023**, *35*, 2300911.
[17] L. Pi, P. Wang, S.-J. Liang, P. Luo, H. Wang, D. Li, Z. Li, P. Chen, X. Zhou, F. Miao, *Nat. Electron.* **2022**, *5*, 248.
[18] W. Kim, H. Kim, T. J. Yoo, J. Y. Lee, J. Y. Jo, B. H. Lee, A. A. Sasikala, G. Y. Jung, Y. Pak, *Nat. Commun.* **2022**, *13*, 720.
[19] Z. Gao, R. Jiang, M. Deng, C. Zhao, Z. Hong, L. Shang, Y. Li, L. Zhu, J. Zhang, J. Zhang, *Adv. Mater.* **2024**, *36*, 2401585.
[20] A. Abnavi, R. Ahmadi, H. Ghanbari, D. Akinwande, M. M. Adachi, *ACS Nano* **2024**, *18*, 34147.

[21] A. Podborska, M. Suchecki, K. Mech, M. Marzec, K. Pilarczyk, K. Szaciłowski, *Nat. Commun.* **2020**, *11*, 854.
[22] D. Nam, J.-U. Lee, H. Cheong, *Sci. Rep.* **2015**, *5*, 17113.
[23] H. Ghanbari, A. Abnavi, R. Ahmadi, M. R. Mohammadzadeh, M. Fawzy, A. Hasani, M. M. Adachi, *Adv. Opt. Mater.* **2024**, *12*, 2401682.
[24] A. Abnavi, R. Ahmadi, H. Ghanbari, M. Fawzy, A. Hasani, T. De Silva, A. M. Askar, M. R. Mohammadzadeh, F. Kabir, M. Whitwick, *Adv. Funct. Mater.* **2023**, *33*, 2210619.
[25] A. Abnavi, R. Ahmadi, A. Hasani, M. Fawzy, M. R. Mohammadzadeh, T. De Silva, N. Yu, M. M. Adachi, *ACS Appl. Mater. Interfaces* **2021**, *13*, 45843.
[26] X. Wang, B. Wang, Q. Zhang, Y. Sun, E. Wang, H. Luo, Y. Wu, L. Gu, H. Li, K. Liu, *Adv. Mater.* **2021**, *33*, 2102435.
[27] Y. Wang, L. Yin, W. Huang, Y. Li, S. Huang, Y. Zhu, D. Yang, X. Pi, *Adv. Intelligent Syst.* **2021**, *3*, 2000099.
[28] N. Ilyas, J. Wang, C. Li, D. Li, H. Fu, D. Gu, X. Jiang, F. Liu, Y. Jiang, W. Li, *Adv. Funct. Mater.* **2022**, *32*, 2110976.
[29] X. Ren, X. He, Z. Duan, X. An, Y. Li, F. Gao, J. Zhang, P. Hu, *ACS Photonics* **2024**, *11*, 4990.
[30] J. R. Nicholls, S. Dimitrijev, P. Tanner, J. Han, *IEEE Trans. Electron Devices* **2019**, *66*, 1675.
[31] W. Wu, L. Wang, R. Yu, Y. Liu, S.-H. Wei, J. Hone, Z. L. Wang, *Adv. Mater* **2016**, *28*, 8463.
[32] H.-Y. Chen, K.-W. Liu, X. Chen, Z.-Z. Zhang, M.-M. Fan, M.-M. Jiang, X.-H. Xie, H.-F. Zhao, D.-Z. Shen, *J. Mater. Chem. C* **2014**, *2*, 9689.
[33] M. M. Islam, D. Dev, A. Krishnaprasad, L. Tetard, T. Roy, *Sci. Rep.* **2020**, *10*, 21870.
[34] M. M. Islam, M. S. Rahman, H. Heldmyer, S. S. Han, Y. Jung, T. Roy, *npj 2D Mater. Appl.* **2024**, *8*, 21.
[35] R. Jana, S. Ghosh, R. Bhunia, A. Chowdhury, *J. Mater. Chem. C* **2024**, *12*, 5299.
[36] Y. Wang, Y. Zhu, Y. Li, Y. Zhang, D. Yang, X. Pi, *Adv. Funct. Mater.* **2022**, *32*, 2107973.
[37] C. Han, X. Han, J. Han, M. He, S. Peng, C. Zhang, X. Liu, J. Gou, J. Wang, *Adv. Funct. Mater.* **2022**, *32*, 2113053.
[38] H. K. Li, T. Chen, P. Liu, S. Hu, Y. Liu, Q. Zhang, P. S. Lee, *J. Appl. Phys.* **2016**, *119*, 244505.
[39] K. Liu, T. Zhang, B. Dang, L. Bao, L. Xu, C. Cheng, Z. Yang, R. Huang, Y. Yang, *Nat. Electron.* **2022**, *5*, 761.
[40] K. Liu, B. Dang, T. Zhang, Z. Yang, L. Bao, L. Xu, C. Cheng, R. Huang, Y. Yang, *Adv. Mater.* **2022**, *34*, 2108826.
[41] M. Dai, X. Zhang, Q. J. Wang, *Adv. Funct. Mater.* **2024**, *34*, 2312872.
[42] Y. Fu, X. Hu, Q. Gong, *Phys. Lett. A* **2013**, *377*, 329.
[43] M. Kaur, S. Kakar, D. Mandal, in *Electromagnetic interference*, 2011 3rd International Conference on Electronics Computer Technology, IEEE: **2011**, pp 1–5.
[44] W. Kim, D. Ahn, M. Lee, N. Lim, H. Kim, Y. Pak, *Small Science* **2024**, *4*, 2400264.
[45] Y.-X. Hou, Y. Li, Z.-C. Zhang, J.-Q. Li, D.-H. Qi, X.-D. Chen, J.-J. Wang, B.-W. Yao, M.-X. Yu, T.-B. Lu, *ACS Nano* **2020**, *15*, 1497.
[46] G. Liu, F. Guo, M. Zhang, Y. Liu, J. Hao, W. Yu, S. Li, B. Hu, B. Zhang, L. Hao, *ACS Appl. Mater. Interfaces* **2023**, *15*, 29375.
[47] C. Pan, C.-Y. Wang, S.-J. Liang, Y. Wang, T. Cao, P. Wang, C. Wang, S. Wang, B. Cheng, A. Gao, *Nat. Electron.* **2020**, *3*, 383.
[48] C. M. Yang, T. C. Chen, D. Verma, L. J. Li, B. Liu, W. H. Chang, C. S. Lai, *Adv. Funct. Mater.* **2020**, *30*, 2001598.
[49] D. Chen, Y.-C. Chen, G. Zeng, Y.-C. Li, X.-X. Li, D. Li, C. Shen, N. Chi, B. S. Ooi, D. W. Zhang, *Nano Res.* **2023**, *16*, 5503.
[50] X. Xu, T. Guo, H. Kim, M. K. Hota, R. S. Alsaadi, M. Lanza, X. Zhang, H. N. Alshareef, *Adv. Mater.* **2022**, *34*, 2108258.